



Multidimensional visualization of the dynamic evolution of Li metal via in situ/operando methods

Shuangyan Lang^a, Michael Colletta^b 📵, Mihail R. Krumov^a, Jeesoo Seok^a, Lena F. Kourkoutis^{b.c} 📵, Rui Wen^{d.e.1}, and Héctor D. Abruña^{a.1} 📵

Contributed by Héctor D. Abruña; received December 2, 2022; accepted January 12, 2023; reviewed by Joaquín Rodríguez-López and Kim See

The growing demands for high-energy density electrical energy storage devices stimulate the coupling of conversion-type cathodes and lithium (Li) metal anodes. While promising, the use of these "Li-free" cathodes brings new challenges to the Li anode interface, as Li needs to be dissolved first during cell operation. In this study, we have achieved a direct visualization and comprehensive analysis of the dynamic evolution of the Li interface. The critical metrics of the interfacial resistance, Li growth, and solid electrolyte interface (SEI) distribution during the initial dissolution/deposition processes were systematically investigated by employing multidimensional analysis methods. They include three-electrode impedance tests, in situ atomic force microscopy, scanning electrochemical microscopy, and cryogenic scanning transmission electron microscopy. The high-resolution imaging and real-time observations show that a loose, diffuse, and unevenly distributed SEI is formed during the initial dissolution process. This leads to the dramatically fast growth of Li during the subsequent deposition, deviating from Fick's law, which exacerbates the interfacial impedance. The compactness of the interfacial structure and enrichment of electrolyte species at the surface during the initial deposition play critical roles in the long-term stability of Li anodes, as revealed by operando confocal Raman spectroscopic mapping. Our observations relate to ion transfer, morphological and structural evolution, and Li (de)solvation at Li interfaces, revealing the underlying pathways influenced by the initial dissolution process, which promotes a reconsideration of anode investigations and effective protection strategies.

lithium metal anodes | deposition/dissolution | in situ/operando methods

Carbon neutrality has become a global imperative to combat the climate crisis. Achieving this will require more aggressive measures to dramatically cut greenhouse gas emissions and transition to clean energy sources. Numerous efforts have been devoted to developing new electrical energy storage devices/technologies to surpass the limits of Li-ion batteries (1, 2). Lithium metal batteries represent promising candidates due to their highly negative potential (-3.04 V vs. standard hydrogen electrode) and exceptionally high theoretical specific capacity (3,856 Ah kg⁻¹) of the Li anode; a value that is over 10 times that of the graphite anode found in current Li-ion technologies (3, 4). When considering alternative cathode materials, efforts have gradually shifted from Li-containing cathodes (such as LiFePO₄ and LiNiCoMnO₂) to high-energy density "Li-free" cathodes (such as sulfur and oxygen) that are based on conversion mechanisms (5). This brings new challenges related to the dynamic evolution and interfacial reactions at the surface of the Li electrode. Pairing a Li metal anode with a Li-free cathode implies that such batteries are assembled in the charged state. During battery discharge, the dissolution of Li metal occurs. This process releases Li ions that migrate to the cathode to facilitate the conversion reactions (6, 7). The initial dissolution (I-Dis) process is critical and significantly influences many important metrics of the interfacial performance at the Li metal anode in subsequent cycles, such as the ion transfer rate, morphological uniformity, conductivity distribution, etc.

Li undergoes repeated dissolution and deposition cycles during cell operation. The reversibility of Li dissolution/deposition processes and the interfacial roughness are highly dependent on the homogeneity and distribution of the solid interfacial interface (SEI) which forms on the surface of the bulk Li via chemical/electrochemical reactions between the Li metal and electrolyte components. The microstructures at the Li/SEI and SEI/ electrolyte interfaces, and the ionic resistance and transport inside the SEI play key roles in the morphological evolution during Li deposition/dissolution (8-11). A defect free, smooth Li surface, coupled with a homogeneous SEI (ideally ionically conducting but electrically insulating) is the prerequisite for uniform Li growth. In addition, Li ion solvation structures and the dynamic (de)solvation processes upon cycling can significantly affect ion interactions in the electrolyte and electrochemical reactions at the interfaces. These processes have attracted increasing attention in recent years in an effort to relate their effects to electrode performance (12, 13).

Significance

We present a systematic investigation of the dynamic evolution of Li interfaces via operando visualization tools. In situ AFM and SECM enable mapping the morphological evolution of the Li metal and the SEI during the initial deposition/ dissolution processes. They show dramatically fast Li growth and a nonuniformly distributed SEI when Li is initially dissolved, causing a significant interfacial impedance and cycling deterioration in subsequent cycles. Employing operando confocal Raman mapping, we found that the real-time decomposition of salt anions and the release of solvent fragments during the initial deposition are key to stabilizing the interface, likely via stable SEI formation. Our results provide fundamental insights into Li dissolution/ deposition dynamics and the development of operando visualization for advanced electrical energy storage devices.

Author contributions: S.L. and H.D.A. designed research; S.L., M.C., and M.R.K. performed research; S.L., M.C., M.R.K., J.S., L.F.K., and R.W. contributed new reagents/ analytic tools; S.L., M.C., M.R.K., L.F.K., R.W., and H.D.A. analyzed data; and S.L., M.C., L.F.K., and H.D.A. wrote the

Reviewers: J.R.-L., University of Illinois Urbana-Champaign; and K.S., California Institute of Technology.

The authors declare no competing interest.

Copyright © 2023 the Author(s). Published by PNAS. This article is distributed under Creative Commons Attribution-NonCommercial-NoDerivatives License 4.0 (CC BY-NC-ND).

¹To whom correspondence may be addressed. Email: ruiwen@iccas.ac.cn or hda1@cornell.edu.

This article contains supporting information online at https://www.pnas.org/lookup/suppl/doi:10.1073/pnas. 2220419120/-/DCSupplemental.

Published February 7, 2023.

The utilization of Li-free cathodes has added new challenges regarding interfacial stability and performance at the Li anode due to the I-Dis process. Using three-electrode cells, Kasemchainan et al. separated deposition from dissolution processes at the Li/solid electrolyte interfaces, underscoring that the larger polarization during dissolution plays a dominant role in triggering dendrite formation upon subsequent deposition (14). The asymmetry in the voltage profiles between initial deposition (I-Dep) and dissolution cases is closely linked to the full-life cycling performance of the Li metal anode (15-17). Recent studies have reported that pitting phenomena frequently occur on multiple sites during Li dissolution, which can degrade the morphological uniformity and exacerbate polarization losses (18-21). Thorough and comprehensive insights into the dynamics of the Li dissolution process require the use of operando methods in order to 1) visualize the interface(s) inside working cells, 2) elucidate how pits, dendrites, SEI, species in solution, and Li solvated structures evolve, and 3) establish the differences under different deposition and dissolution sequences. This is necessary to identify performance limiting processes and develop solutions that will enable the transition to Li-free cathode materials.

In this study, using Li-S cells as a model system, we investigate the differences in the Li interfaces during dissolution and deposition processes, through complementary characterization methods including electrochemical impedance spectroscopy (EIS), in situ atomic force microscopy (AFM), scanning electrochemical microscopy (SECM), cryogenic scanning transmission electron microscopy (cryo-STEM), electron energy-loss spectroscopy (EELS), and operando confocal Raman imaging. The use of three-electrode cells enables decoupling the contributions from individual electrodes. It was found that the overall resistance in Li-S batteries is predominantly controlled by the Li metal anode. The interface present during the I-Dis process exhibits larger and unevenly distributed interfacial resistances, compared with the I-Dep one, which continues to influence the subsequent deposition/dissolution processes. Morphological evolution was monitored for both cases using in situ AFM. Rapid dendritic Li growth was observed after the first dissolution process, accompanied by a fast increase of the interfacial roughness and possible breaks of the SEI. SECM enables mapping the compactness and distribution of the SEI, providing direct evidence that the SEI exhibits a higher electronic conductivity and reduced uniformity when Li is first dissolved. A more compact and evenly distributed SEI is formed during the I-Dep as indicated by cryo-STEM EELS. Additionally, the evolution of different electrolyte species that react with Li during I-Dep and I-Dis were visualized in real time by operando Raman imaging. The increased concentration of the Li salt and solvent fragments near the Li electrode surface during the I-Dep process play key roles in the interfacial regulation, enabling a stable and uniform interface formation for subsequent cycles. In contrast, it is much more difficult to modify the interface during the I-Dis process, which illustrates the underlying reasons for the rough and heterogeneous interface when Li is first dissolved. This emphasizes the importance of interfacial stabilization during the initial Li dissolution process. By combining multidimensional characterization techniques, we have achieved a detailed understanding of the Li interfaces undergoing different deposition/dissolution processes. These could, in turn, systematically provide insights into the interfacial mechanisms of the resistance and morphological evolution, SEI distribution, electrolyte decomposition, and Li solvation processes, providing fresh impetus to reconsider anode protection during the dissolution process.

Results and Discussion

Identifying Impedance Contributions Using Three-Electrode Cells. In an effort to separate the contributions of the Li metal anode from overall interfacial processes inside Li-S batteries, a three-electrode cell was employed where the current passes between the working electrode (WE) and counter electrode (CE), while the potential changes of the WE and CE are measured with respect to a reference electrode (RE). Fig. 1A presents a schematic illustration of the three-electrode cell setup. A homogeneous slurry of sulfur: polyvinylidene fluoride: super P (8:1:1) coated onto carbon paper was employed as the WE. Li foil was used as CE and RE. 1.0 M lithium bis(trifluoromethanesulfonyl)imide (LiTFSI) in 1,3-dioxolane (DOL)/1,2-dimethoxyethane (DME) (1:1) was used as the supporting electrolyte. A cyclic voltammetric (CV) profile performed in the three-electrode cell is shown in SI Appendix, Fig. S1.

EIS measures the faradic impedance to a small amplitude sinusoidal voltage excitation as a function of excitation frequency. From an analysis of the real and imaginary impedance components one can extract the heterogeneous charge transfer parameters allowing quantification of complex interfacial phenomena. Fig. 1B displays the Nyquist plots of the S/electrolyte and Li/electrolyte interfaces during the first cycle in a three-electrode cell. Nyquist plots of the C/Li₂S₈ electrolyte interfaces are shown in SI Appendix, Fig. S2. These indicate that the separation of the semicircles at the S interface (Fig. 1 B, Left) can be related to the deposition of sulfide species. The technique of distribution of relaxation times (DRT) was used to transform the frequency domain-based Nyquist plots into time domain-based DRT spectra, with the aim of distinguishing/separating the specific electrochemical processes (Fig. 1C) (22, 23). In the spectra obtained for the S electrode, three major peaks located in the 10⁻⁵, 10⁻², and 10-s regions were observed. These can be roughly attributed to the solution resistance, charge transfer at the C/electrolyte interface, and charge transfer at the S/electrolyte interface, respectively. SI Appendix, Fig. S3 shows the schematics of the S and Li interfaces. The split of the peak in the 1- to 10-s region during the discharge process is due to the lithiation of S, corresponding to the increase of the second semicircle (the one at low frequency) in the Nyquist plot.

In comparison, the DRT spectra of the Li electrode exhibit a much more complex impedance distribution with larger values. The evident split and resistance increase in the peaks in the regions of 10^{-5} to 10^{-3} s and 10^{-2} to 10 s indirectly reflect the heterogeneity of the interfacial morphology, conductivity and SEI distribution at Li interfaces during the discharge/charge reactions. We further employed equivalent circuits to analyze the impedance evolution at the two electrodes (SI Appendix, Fig. S4). The values of the resistances at the S and Li interfaces are shown in Fig. 1D, with R₁, R₂, and R₃ representing the solution resistance and charge transfer resistances at the conductive agent/electrolyte and the deposited product/electrolyte interfaces, respectively. In the Li case, R₂ and R₃ are combined to represent the resistances at the Li and SEI/electrolyte interfaces. The results are consistent with the DRT analysis, which exhibits larger values of interfacial resistances at the Li metal, revealing that the major contribution to the overall cell resistance and interfacial heterogeneity comes from the Li/electrolyte interfaces.

Furthermore, using a three-electrode Li-Li-Li cell, we analyzed the evolution of interfacial impedances at the Li/electrolyte interfaces during the electrodeposition and dissolution processes; 50 mM Li₂S₈ was added to the electrolyte, forming a sulfide-rich SEI layer similar to the case in Li-S batteries. Fig. 1E presents the Nyquist plots at the WE-Li (I-Dis) and

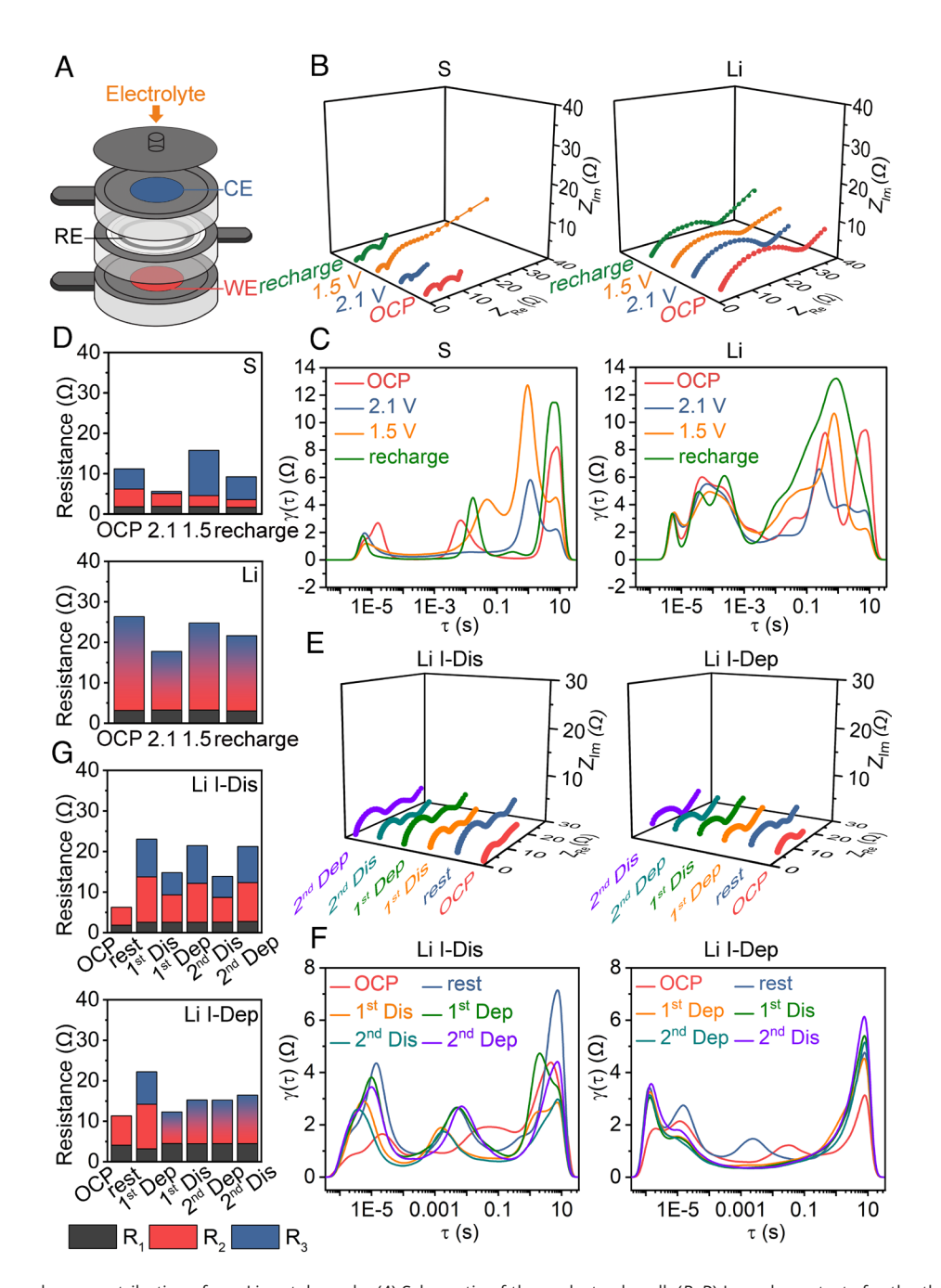


Fig. 1. Separating impedance contributions from Li metal anode. (A) Schematic of three-electrode cell. (B-D) Impedance tests for the three-electrode Li-S-Li cell (electrolyte: 1 M LiTFSI in DOL/DME). (B) Nyquist plots of the S/electrolyte and Li/electrolyte interfaces at different stages of the initial discharge and recharge processes. (C) DRT spectra transformed from the Nyquist plots in B. (D) Values of the interfacial resistances fitted to the equivalent circuit at the S/electrolyte and Li/electrolyte interfaces, respectively. We combined the values of R2 and R3 in the Li case since only one extended semicircle was observed in the Nyquist plots in B. (E-G) Impedance tests for the three-electrode Li–Li-Li cell (electrolyte: 50 mM Li₂S₈, 1 M LiTFSI in DOL/DME). (E) Nyquist plots of the WE-Li/electrolyte interfaces (I-Dis) and the CE-Li/electrolyte interfaces (I-Dep) during galvanostatic dissolution and deposition processes at a current density of 3.0 mA cm⁻² using a threeelectrode Li cell. Li would be deposited onto the CE when it is dissolved from the WE. (A) DRT spectra transformed from the Nyquist plots in E. (G) Corresponding values of the resistances fitted to the equivalent circuit at the I-Dis and I-Dep Li/electrolyte interfaces, respectively. For the I-Dep case, the values of R2 and R3 were combined after the first deposition process due to the merging of the semicircles in the Nyquist plots. R₁, R₂, and R₃ in D and G represent the interfacial resistances fitted to the equivalent circuit shown in SI Appendix, Fig. S4. In B and E, the dots are raw data, and the connecting lines are fitting curves from the equivalent circuit.

CE-Li/electrolyte (I-Dep) interfaces. A small semicircle can be observed at both WE and CE after cell assembly (red). After resting at open circuit (OCP) for 150 min (blue), an additional semicircle is formed due to the formation of the SEI at the OCP. The voltage-time curves during the electrodissolution and deposition processes are shown in SI Appendix, Fig. S5. We acquired Nyquist plots for both WE and CE after every half cycle. The Nyquist plots show two semicircles at the WE-Li/ electrolyte interfaces, where Li is dissolved first, while they

merge into one after the first deposition process at the CE-Li/ electrolyte interfaces. We refer to this as the "lips phenomenon," with two curves on the upper side and one on the bottom. This lips phenomenon, that shows the larger resistances and heterogeneities of the first-dissolved Li, remain after the subsequent dissolution/deposition and cycling (green, cyan, and purple curves in Fig. 1E), confirming the important role of the deposition/dissolution sequence on the long-term performance, as previously reported (15, 16).

Fig. 1F shows the DRT transformations of the Nyquist plots. On both electrodes, the formation of the SEI after resting leads to an increase of all the peaks at different relaxation times. For the I-Dis electrode, the peak at 1 to 10 s clearly splits after the first dissolution process, significantly increasing during the subsequent reactions, which can be due to morphological changes such as pit formation, dendritic Li growth, etc. However, for the I-Dep process, the peak in the middle relaxation time $(10^{-3} \text{ to } 10^{-1} \text{ s})$ disappears after the first deposition, with the spectra remaining almost unchanged afterward. Similar phenomena were observed in an electrolyte without polysulfides indicating that their presence is not necessary for observing such phenomena (SI Appendix, Fig. S6). The corresponding values of the resistances fitted to equivalent circuits are presented in Fig. 1 G, showing the larger interfacial resistances and heterogeneities of the I-Dis electrode as well. These differences are attributed to the different morphological evolution at the interfaces, which is further illustrated in the following in situ AFM observations. A schematic, presented in *SI Appendix*, Fig. \$7, provides a detailed explanation.

The kinetics of SEI growth at OCP and the effects of polysulfides were also explored (*SI Appendix*, Fig. S8). The linear relationship of the resistance vs. time ¹⁷² plot suggests a diffusion-controlled process. Further analysis reveals that the SEI growth rate decreased after adding the polysulfides; illustrating the polysulfides' benefits for Li interfacial modification and SEI stabilization.

In situ AFM Study of the I-Dis Process on Li Morphological Evolution. To better understand the large resistance from the standpoint of the morphological evolution, we employed in situ AFM to monitor the Li growth processes in real time when Li was first deposited or dissolved. Fig. 2A provides a schematic of the three-electrode Li-Li-Li cell used for the in situ AFM study. Fig. 2B shows the voltage trace during the first deposition process at a current density of 3.0 mA cm⁻². Fig. 2C provides the AFM images captured at different reaction states of the first deposition process, as marked on Fig. 2B. When Li is first deposited (Fig. 2C and Movie S1), a Li island of about 5 μm, was observed at 20 min as marked in the P1 AFM image. This Li island gradually expanded from the surface over the next 20 min. In addition, some small protrusions evolved/grew in the surrounding areas as shown in image P2. After 1 h of deposition (a specific capacity of 3.0 mAh cm⁻², image P3), the size and shape of the island remained essentially the same. The changes in its volume could be approximately measured as the reaction proceeded, which indicated that the growth rate significantly decreased in the later stages (SI Appendix, Fig. S9). As shown in Fig. 2D, the evolution of the interfacial roughness exhibited

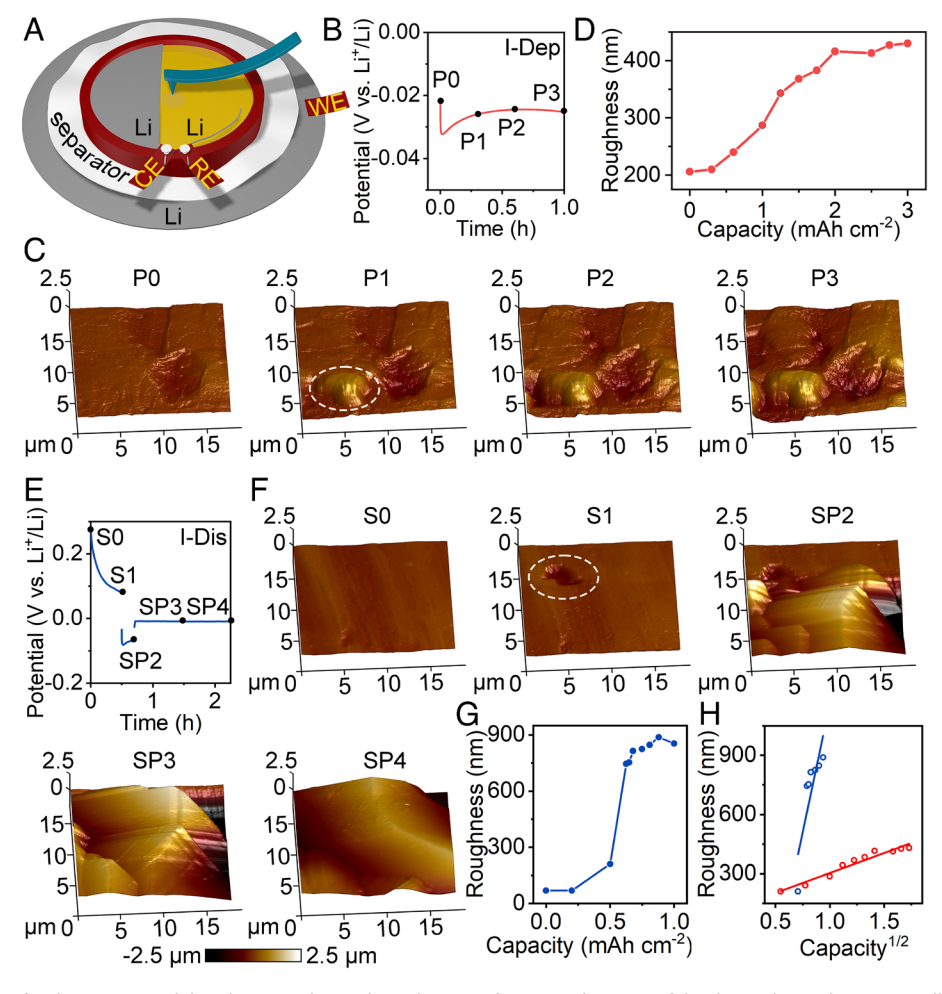


Fig. 2. In situ AFM study of Li deposition and dissolution at the Li/electrolyte interface. (A) Schematic of the three-electrode Li-Li-Li cell (electrolyte: 50 mM Li₂S₈, 1 M LiTFSI in DOL/DME). (*B*) Voltage trace of the galvanostatic I-Dep process at a current density of 3.0 mA cm⁻². (C) AFM images of the Li metal during the first deposition process with images taken every 20 min. (*D*) Quantification of the roughness evolution during the first deposition process. (*E*) Voltage trace for the I-Dis case (first dissolution and the subsequent deposition), at 3.0 mA cm⁻² dissolution for 0.5 h; and 3.0 mA cm⁻² then 0.25 mA cm⁻² deposition for 750 s and 5,400 s, respectively. (*F*) Corresponding AFM images of the Li metal at different reaction states as marked on *E*. (*G*) Quantification of the roughness evolution for the I-Dis case. (*H*) Linear fitting of the roughness to the square root of the capacity for both I-Dep ($R^2 = 0.944$) and I-Dis ($R^2 = 0.671$) cases.

a similar trend as the volume change of the island; that is, an initial growth followed by a plateau. A clear linear relationship was observed between the roughness and the square root of the capacity (red curve in Fig. 2H), indicating a diffusion-controlled Li growth process. This kind of surface growth model implies a balanced relationship between the rates of SEI formation and Li deposition, which avoids forming deleterious Li dendrites (24, 25). After the subsequent dissolution process, small SEI clusters could be clearly observed on the Li island (*SI Appendix*, Fig. S10), suggesting that the SEI is dynamically growing and can remain, at least partially, during the I-Dep process.

In contrast, Fig. 2 *E*–*G* and Movie S2 present the in situ visualization of Li metal interfaces when Li is first dissolved. Fig. 2E shows the voltage trace of the first dissolution and the following deposition processes. The AFM images in Fig. 2F show the morphological evolution at different reaction states marked on Fig. 2E. The pristine Li surface, before reactions, is shown in image S0. After applying a current density for dissolution of 3.0 mA cm⁻² for 0.5 h, a large pit was found at the surface, as circled out in image S1. *SI Appendix*, Fig. S11 provides 50-μm × 50-μm images, which indicate that pits form in multiple regions. Upon switching the polarity (deposition after dissolution), a number of Li branches grew out of the bulk Li during the initial 750 s with a specific capacity of 0.625 mAh cm⁻² (image SP2). A smaller current density of 0.25 mA cm⁻² was then applied for detailed observation. During the subsequent deposition process, to a capacity of 1.0 mAh cm⁻², the sizes of the Li branches increased, merged into large clusters, and covered almost all of the pristine surface that was initially observed (images SP3 and SP4). Fig. 2G shows the corresponding quantification of the interfacial roughness. A comparison of the roughness fittings for both cases is presented in Fig. 2H. For the I-Dis case, a rapid and significant increase in the interfacial roughness clearly deviates from Fick's law (blue curve in Fig. 2H), which can be due to excess of Li ions near the surface and the localized break of the SEI. This in situ AFM imaging confirms our findings from impedance testing, revealing that the morphological evolution during the dissolution process can significantly interrupt the uniform Li growth. SECM was then employed to understand, in detail, the effects of I-Dis on the conductivity and distribution of the SEI.

Comparison of the SEI Compactness and Uniformity by SECM and Cryo-STEM EELS. SECM is a powerful tool for the analysis of surface conductivity, providing complementary information on the topographical evolution from AFM observations. The cell configuration of the SECM test was similar to that used for the in situ AFM study: a three-electrode Li-Li-Li cell for performing the Li dissolution/deposition reactions. However, it needs to be emphasized that the working principle is different. The SECM experiment utilizes an ultra-micro electrode (UME) as the probe, which records the Faradic current of an electroactive species (known as a redox mediator) as it interacts with the substrate, enabling a chemically selective probe of the local electrochemical activity (26–28). Fig. 3A shows the hemispherical diffusion of the mediator to the tip far away from the substrate.

Feedback from the substrate is reflected by the perturbation of the redox current when the tip approaches the substrate surface. As shown in Fig. 3B, when the tip is brought near a conductive substrate, regeneration of the mediator occurs via nonlocal electron transfer-driven concentration gradients near the probe. The resulting increase in the flux of the mediator to the probe causes an increase in the measured current, termed positive feedback. In contrast, an insulating substrate blocks the diffusion decreasing transport of the mediator and results in a lower current at the

probe (negative feedback, Fig. 3C). The approach curves, plots of the normalized tip current vs. tip-to-substrate distance, respectively, representing the positive and negative feedbacks are shown in Fig. 3 D and E, respectively. Note that the polysulfides in the electrolyte are oxidized to elemental sulfur at potentials positive of 2.7 V, similarly at potentials negative of 2.3 V the polysulfides are reduced to Li₂S₂/Li₂S, fouling the probe. Methyl viologen (MV²⁺), with a reduction potential of 2.4 V vs. Li⁺/Li, was chosen as the mediator to avoid the redox processes of the polysulfides in solution. A schematic of the reaction potentials is presented (SI Appendix, Fig. S12) for clearer explanation/understanding.

We first employed a stainless-steel substrate to calibrate the setup by adjusting the tilt (SI Appendix, Fig. S13). Afterward, a flat and fresh piece of Li foil was secured on top using double-sided Cu tape. The CV profiles measured on top of the Li and stainless-steel substrates are shown in SI Appendix, Fig. S14A. They both show an anodic current positive of 2.4 V, which could be due, at least in part, to the side reactions between MV2+ and the electrolyte. Resting at OCP, the reactions would reach equilibrium. The differences in the current responses when the tip approaches the substrate provide a measure of the local conductivity, which indicates the distribution and heterogeneity of the SEI (29-31). As shown in the approach curve in SI Appendix, Fig. S14B, the current remains constant as the tip approaches the Li, and then shows an evident drop as it reaches the SEI region. Fig. 3 F and G present the in situ scans of the SEI evolution when Li is first deposited or dissolved, respectively. For both cases, negative feedbacks throughout the surface were detected homogeneously in a $200 \times 200 \,\mu\text{m}^2$ region before applying any current, showing that the SEI is formed at OCP via chemical reactions. To mitigate the influence of the surface height differences, we employed a smaller current density of 0.5 mA cm⁻² for Li deposition and dissolution. As Li is first deposited, more regions exhibiting negative feedback were observed on the left side (marked as I in the 10-min image of Fig. 3F), which reveals the further growth of the SEI under negative potentials. The current increase during the remaining 20 min of Li deposition can be related to the thinning of the SEI layer as the volume of the Li electrode grows due to the plated Li beneath the SEI. During the subsequent dissolution process, no evident changes in the average current were detected, even though small local fluctuations were observed. Fig. 3H presents the evolution of the average normalized current and the quantified heterogeneity as the deposition/dissolution proceeded. The cyan line illustrates a completely insulated and uniformly distributed SEI during the I-Dep. However, the uniformity and compactness of the SEI decrease significantly when Li is first dissolved (Fig. 3*G*). Two regions II and III were marked on the image at 10-min dissolution, which, respectively, exhibited a decrease and increase in the local current. This heterogeneity is directly due to the uneven topographical evolution, which remains and is even exacerbated during the remaining 20 min of dissolution. Furthermore, the average normalized current rapidly increased when Li was subsequently deposited. Localized positive feedback was observed (region IV, 60 min image), providing direct evidence of breaks in the SEI layer. The orange curve in Fig. 3H shows the corresponding quantification, indicating a nonuniform and partially destroyed/broken SEI layer for the I-Dis case.

The raw tip currents during the interfacial evolution of the Li metal are provided in SI Appendix, Fig. S15. Supplementary experiments were performed using ferrocene (Fc) as the mediator in an electrolyte without polysulfides. The evident heterogeneities and localized positive regions on the SECM maps clearly show the breaks of SEI layer during the I-Dis-subsequent deposition processes (SI Appendix, Fig. S16). In an effort to verify the

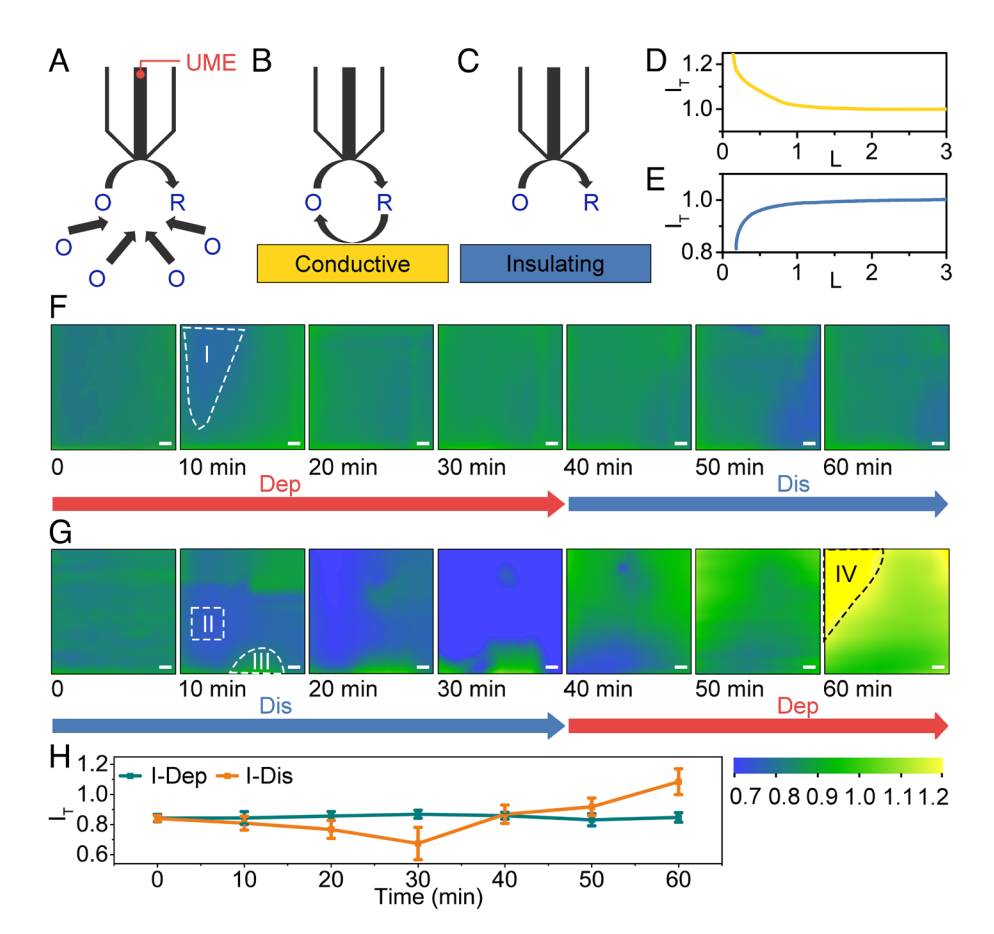


Fig. 3. Investigation of the SEI evolution using SECM. (A–E) SECM working principles. (A) Hemispherical diffusion to an UME probe far from the substrate. (B) Positive feedback at a conductive substrate. (C) Negative feedback blocked by an insulating substrate. (D and E) SECM approach curves at a conductive and insulating substrate, respectively. I_T and L represent the normalized tip current and tip-to-substrate distance. (E and E) In situ scans of SECM maps when L is first deposited and dissolved, respectively (electrolyte: 5 mM MV²⁺, 50 mM Li_2S_8 , 1 M LiTFSI in DOL/DME). Each sequence includes a set of 30-min deposition and dissolution processes. SECM imaging was taken every 10 min. The scale bars are 20 μm. (E) Quantification of the changes of tip current vs. reaction time.

compactness and composition of the SEI, cryo-STEM EELS was carried out on both I-Dis and I-Dep samples.

For high-resolution structural and chemical characterization of the SEI layer in both I-Dep and I-Dis cases, electron transparent cross-sections of the Li-electrolyte interface were prepared using the cryogenic focused ion beam (cryo-FIB) lift-out technique (32, 33). Dendrites were located within each cross-sectional lamella and imaged using both annular dark field (ADF) STEM imaging and EELS elemental mapping (SI Appendix, Fig. S17). Highresolution cryo-STEM imaging shows the dendrite-electrolyte interface. These images alone, however, do not immediately reveal the structure of the SEI layer (Fig. 4 A and D). With the addition of spectroscopic mapping by cryo-STEM EELS (Fig. 4 B and E), we observed a significant increase in the concentration of oxygen along the edges of the lithium dendrite structure. This region of high oxygen counts and low carbon counts, relative to the electrolyte, is indicative of the SEI layer (34). We can see from the elemental maps that the SEI layer is generally more evenly distributed in the I-Dep case compared with the I-Dis case. Elemental concentration profiles across the dendrite-electrolyte interface (Fig. 4 C and F) reveal that the SEI consists of two distinct regions. The inner layer is a compact layer, identified by low lithium and carbon concentrations and a high concentration of oxygen. The outer layer is a diffuse region of the SEI and is identified by decreasing oxygen counts and an increase in carbon concentration. While the inner, compact layer of the SEI in both I-Dep and I-Dis cases is similar in approximate thickness (~120 nm for I-Dep and ~100 nm thick for I-Dis), the outer diffuse region is clearly distinct in both

samples. For the I-Dis dendrite, we see that the diffuse region, containing significant cross-over of carbon and oxygen, is slightly thicker (~110 nm thick) than the corresponding compact region. The outer SEI layer is significantly more abrupt in the I-Dep case, with the diffuse region being about half as thick (~60 nm) as the inner layer. The fine structures of lithium, carbon, and oxygen within the SEI region are shown in *SI Appendix*, Fig. S18. The lithium and oxygen fine structures in both I-Dis and I-Dep cases are nearly identical, and closely match the structure of Li₂O (34). The carbon fine structure shows higher carbonate bonding (C=O) than C–H bonding in the SEI layer. These results indicate an uneven, loose, and diffuse SEI layer on the first dissolved Li, which could be due, at least in part, to the different electrolyte reactions at the Li interface during the I-Dep/I-Dis processes.

Analyzing the Electrolyte Decomposition via Operando Confocal Raman Mapping. To better understand the interfacial reactions involving electrolyte decomposition and Li solvation during the deposition and dissolution processes, we employed operando confocal Raman microscopy to monitor and analyze the real-time changes of different electrolyte components near the Li electrode surface (35, 36). Using a spatial pinhole to block out-of-focus light, confocal microscopy enables imaging of the exact focal plane (Fig. 5 *A, Left*). The coin cell casing was modified for operando observation. As shown in the schematic (Fig. 5 *A, Right*), the edge of the Li that we observe was placed in the middle of the observation window, as marked with a red curve. The yellow region in the observation window indicates the polysulfide electrolyte.

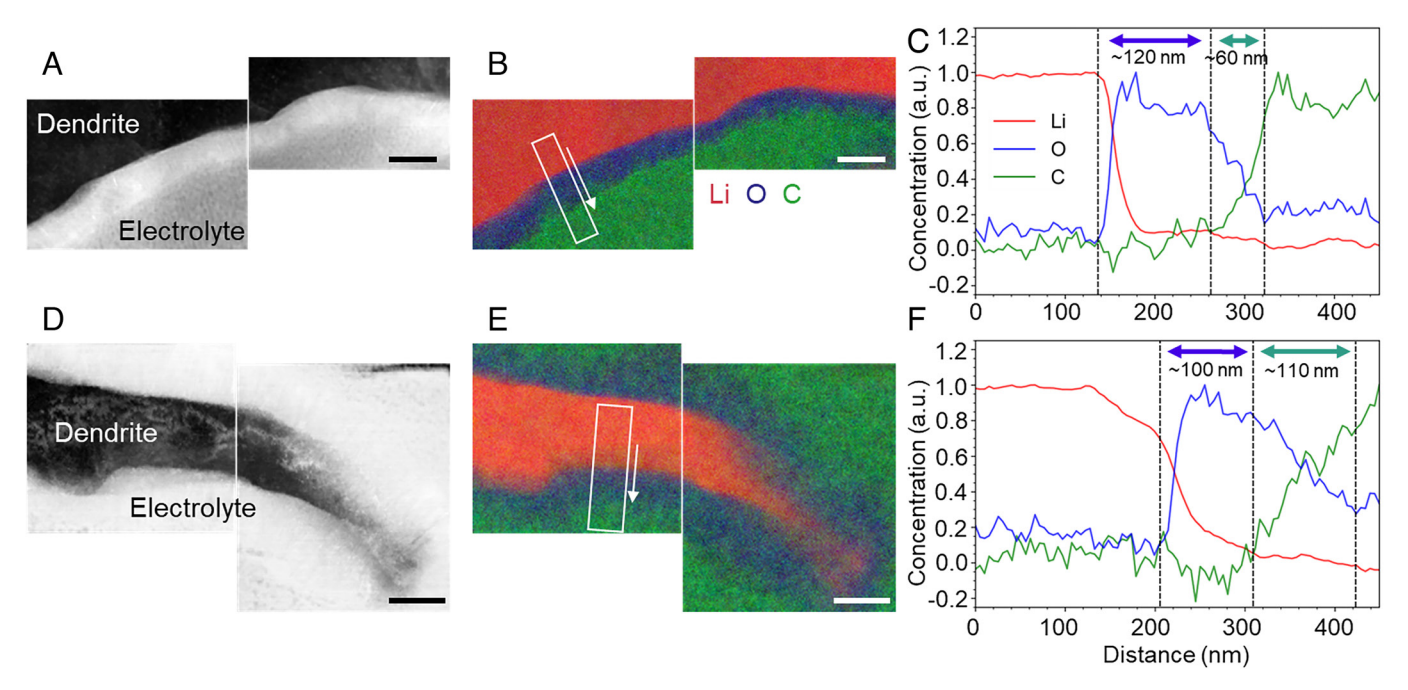


Fig. 4. Cryo-STEM spectroscopy analysis of distinct dendrite-electrolyte interfaces. (A and D) Cryo-ADF-STEM image of lithium dendrite in deposition (A) and dissolution cases (D), respectively. (B and E) Corresponding cryo-STEM-EELS elemental maps, in which lithium, oxygen, and carbon concentrations are mapped as red, blue, and green regions, respectively. (C and F) Elemental concentration profiles of the dendrite-electrolyte interfaces, including lithium, oxygen, and carbon, with the profile regions shown in B and E, respectively. Compact and diffuse layers of the SEI are identified by blue and teal arrows, respectively. Li-Li symmetric coin cells with polysulfide electrolyte (50 mM Li₂S₈, 1 M LiTFSI in DOL/DME) were employed. All scale bars are 200 nm.

We focused on this Li edge and observed the Li deposition/ dissolution process from the cross-sectional direction. A full spectrum of the electrolyte near the Li electrode at OCP is shown in SI Appendix, Fig. S19. Fig. 5B presents the voltage trace when a constant current density of 3.0 mA cm⁻² was applied to drive Li deposition and dissolution. The dynamic evolution of the Raman spectra during deposition and dissolution are shown in Fig. 5C, which tracks the changes in the concentration of polysulfides and LiTFSI at the electrode interfaces. The peak regions at 395, 449, 535, 742, and 1,243 cm⁻¹, which are highlighted in red, orange, yellow, blue, and purple, respectively, are attributed to the stretching vibrations of the central and terminal S–S bonds in S_x^{2-} , the stretching vibration of S-S in S_3^- , the bending vibration of C-N-C bond, and the stretching vibration of CF₃, respectively. Thus, these peaks can be used to represent the different components in the electrolyte solution: long-chain polysulfides (typically S_8^{2-}), intermediate polysulfides (typically S₄²-), S₃⁻, and Li salt (LiTFSI) (37-41). The spectral series shows evident decreases in S_x^{2-} species with a concurrent increase of the LiTFSI concentration at the electrode interfaces.

Fig. 5D presents an overlay of the optical image of Li (Left) and the confocal Raman mapping of the electrolyte near Li (*Right*, red: S_8^{2-} , blue: C-N-C). The optical images during the initial Li deposition processes are shown in SI Appendix, Fig. S20. The local current densities at the edge positions that we are focusing on can be higher than 3.0 mA cm⁻². The extent of Li growth shows a linear relationship with the square root of time, suggesting a diffusion-controlled process. As shown in Fig. 5 E and F, we simultaneously visualized the Li deposition/dissolution from the optical imaging and the changes in electrolyte species near Li from Raman mapping. Similar to the trends from Raman spectra, the intensity of the red regions (long-chain polysulfides) decreases, and that of the blue one (LiTFSI) increases and becomes dominant after the whole deposition and dissolution processes. Fig. 5G presents the quantified evolution of the S_8^{2-} , S₄²⁻, S₃⁻, C-N-C, and CF₃ species in normalized intensities,

derived from the operando Raman mapping results. The intensities of the polysulfides continuously decreased during the whole deposition and dissolution processes, which is due to reduction of polysulfides at the electrode forming short-chain sulfides including S₃-. Interestingly, the intensities of the LiTFSI fragments, C-N-C and CF3, significantly increase during the first deposition process, while change only slightly during the subsequent dissolution process. We believe that this reflects the fact that during Li deposition TFSI can be reduced (and form part of the SEI) while during the subsequent dissolution, such processes are unlikely, which can be related, at least in part, to the stronger interaction with Li ions of TFSI- when compared with S_x^{2-} (SI Appendix, Fig. S21).

Fig. 5H shows the quantified evolution of the polysulfides and Li salt fragments during the I-Dis process. The corresponding spectra, and optical images combined with operando mappings are presented in SI Appendix, Fig. S22. The intensity of the polysulfides decreases during the whole dissolution and deposition processes, which is consistent with the case when Li is first deposited. However, the decomposition of LiTFSI is evidently suppressed during the deposition after the first dissolution process. We further studied these phenomena with X-ray photoelectron spectroscopy (XPS) (SI Appendix, Fig. S23). The C1s spectra show an evident higher ratio of CF_3 on the I-Dep sample, revealing the higher intensity of LiTFSI. In addition, the elemental ratios of C and O are higher for the I-Dis case from the analysis of atomic distribution. The higher amounts of organic fragments and lower of LiTFSI would lead to an organic-rich, diffuse SEI, which agrees with the STEM-EELS mapping observations. This results in the decreased de-solvation of Li ions during the subsequent deposition process, leading to the suppression of LiTFSI supply, and in turn, restraining the further formation of SEI at Li interfaces under cell operation.

Given the reactions of polysulfides and LiTFSI one may ask, how would the solvent change in real-time during both I-Dep and I-Dis cases? SI Appendix, Fig. S24 presents the ¹⁷O chemical shifts

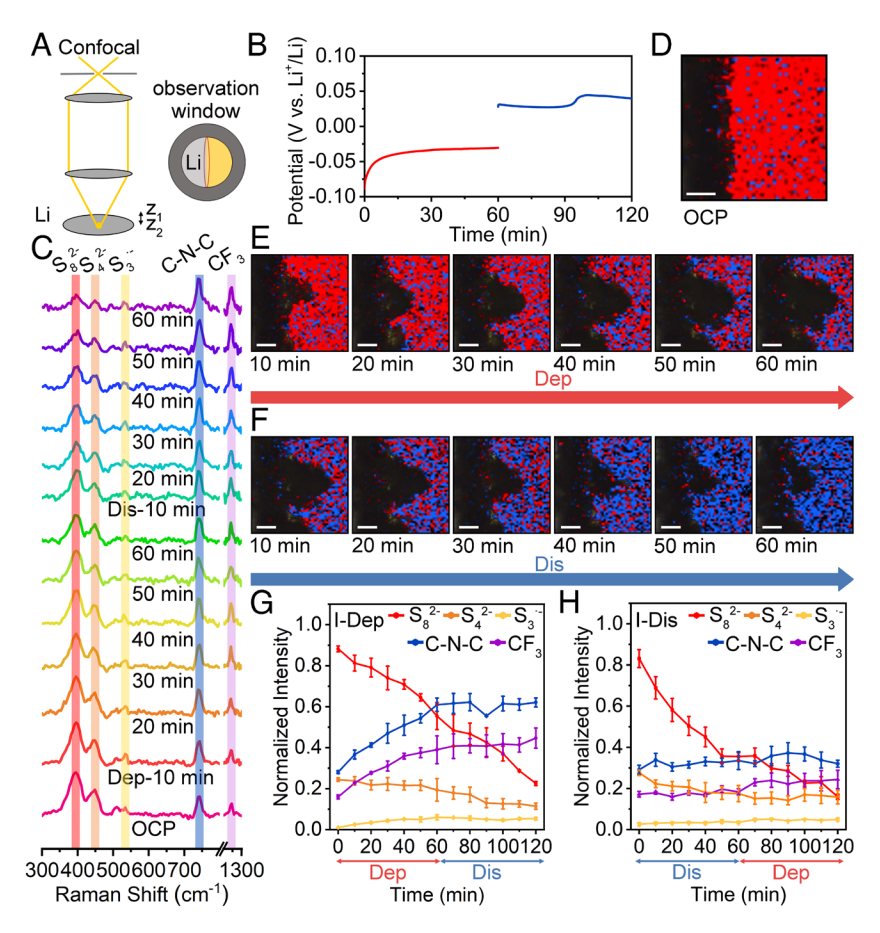


Fig. 5. Operando confocal Raman mapping of Li/electrolyte interfaces (time evolution of the polysulfides and LiTFSI) during Li deposition and dissolution. (A) Schematics of confocal microscopy imaging (*Left*), and the modified coin cell using Li as both electrodes in an electrolyte of 50 mM Li₂S₈, 1 M LiTFSI in DOL/DME (*Right*). (B) Voltage–time curves during the I-Dep and subsequent dissolution. (C) Operando Raman spectra of the electrolyte near the Li metal with 1.0 M LiTFSI and 50 mM Li₂S₈ in DOL/DME. (D) Overlay of the optical image of Li (*Left*) and the confocal Raman mapping of the electrolyte (*Right*) at OCP. (*E* and *F*) Operando scans of the Li/electrolyte interfaces during deposition (*E*) and dissolution (*F*), respectively. In D, E, and F, the red and blue colors represent the intensities of long-chain polysulfides and LiTFSI, respectively. The scale bars are 30 μm. (*G* and *H*) Quantification of the average changes in normalized intensities vs. reaction time during the (*G*) I-Dep and (*H*) I-Dis processes. The SDs were drawn based on three sets of operando measurements.

(from NMR measurements) of the solvents (DOL and DME) when increasing the Li ion concentration in the solution from 0.1 to 2 M. The gradual upfield shifting and broadening of both peaks indicates that both DOL and DME solvents are involved in the Li solvation process (42, 43). In addition, the ¹⁷O shift shows a larger value in DME (from –21.8 to –28.4 ppm) than DOL (from 38.2 to 36.3 ppm), reflecting the stronger interaction of DME with the Li ions due to its bidentate binding ability. We further analyzed the dynamic changes of the solvent from the operando Raman spectra and mappings (Fig. 6). Fig. 6A presents the spectral evolution during the I-Dep and subsequent dissolution processes. The peak regions at 870, 1,138, and 941 cm⁻¹, highlighted in gray, green, and yellow, are ascribed to the stretching vibrations of C–O in DME and C–O/C–C in DOL (40). Distinctive increases can be observed for both peaks at 941 cm⁻¹ (DOL) and 1,138 cm⁻¹ (DME).

The corresponding Raman mappings are presented in Fig. 6 *B* and *C*. Evidently, both solvents exhibit clear increases during the I-Dep process. This increase can be due, at least in part, to the release of free solvent during the Li de-solvation process (44). Quantification of the three peak regions at 870, 1,138, and 941 cm⁻¹, during the whole deposition and dissolution processes, are shown in Fig. 6*D*. Following the I-Dep, the intensities of the solvents remain essentially constant during the subsequent dissolution process. By contrast, the intensities remain low during the whole I-Dis case (Fig. 6*E*), consistent with the reduced Li de-solvation process and the formation of a diffuse SEI layer as discussed above. The spectra and images for

the I-Dis case are presented in *SI Appendix*, Fig. S25. In situ scans of the electrolyte decomposition on the surface of the Li metal (*SI Appendix*, Fig. S26) and the Cu substrate (*SI Appendix*, Fig. S27) show similar trends to the cross-sectional results, further confirming the differences in the evolution of the polysulfides, Li salt, and solvent during different deposition/dissolution processes, providing important clues regarding Li solvation and interfacial stability.

In order to explain, in detail, how the Li salt anions and solvents evolve during the different deposition and dissolution sequences, a schematic is shown in Fig. 6F. For the I-Dep case, due to the larger overpotential and Li de-solvation process during the initial Li deposition, more anions and solvent fragments are formed and accumulated near the Li interface, which serve as supplies/reactants to strengthen the SEI, as observed by operando confocal Raman mapping. During the subsequent dissolution process, the migration of the anions from the bulk electrolyte to the interface can offset their consumption during the Li solvation process, maintaining the compactness of the interfacial structure and the enrichment of electrolyte species near the Li electrode. However, for the I-Dis case, the release of Li ions during the I-Dis process disrupts the uniformity of the interfacial morphology, ion transfer and species distribution according to our observations, which, in turn, leads to a disordered interfacial structure with a diffuse SEI. Li de-solvation through the SEI is significantly decreased during the subsequent deposition process, leaving the interfacial structure disrupted, and susceptible to further degradation during the following cycles. By operando visualization of the different electrolyte

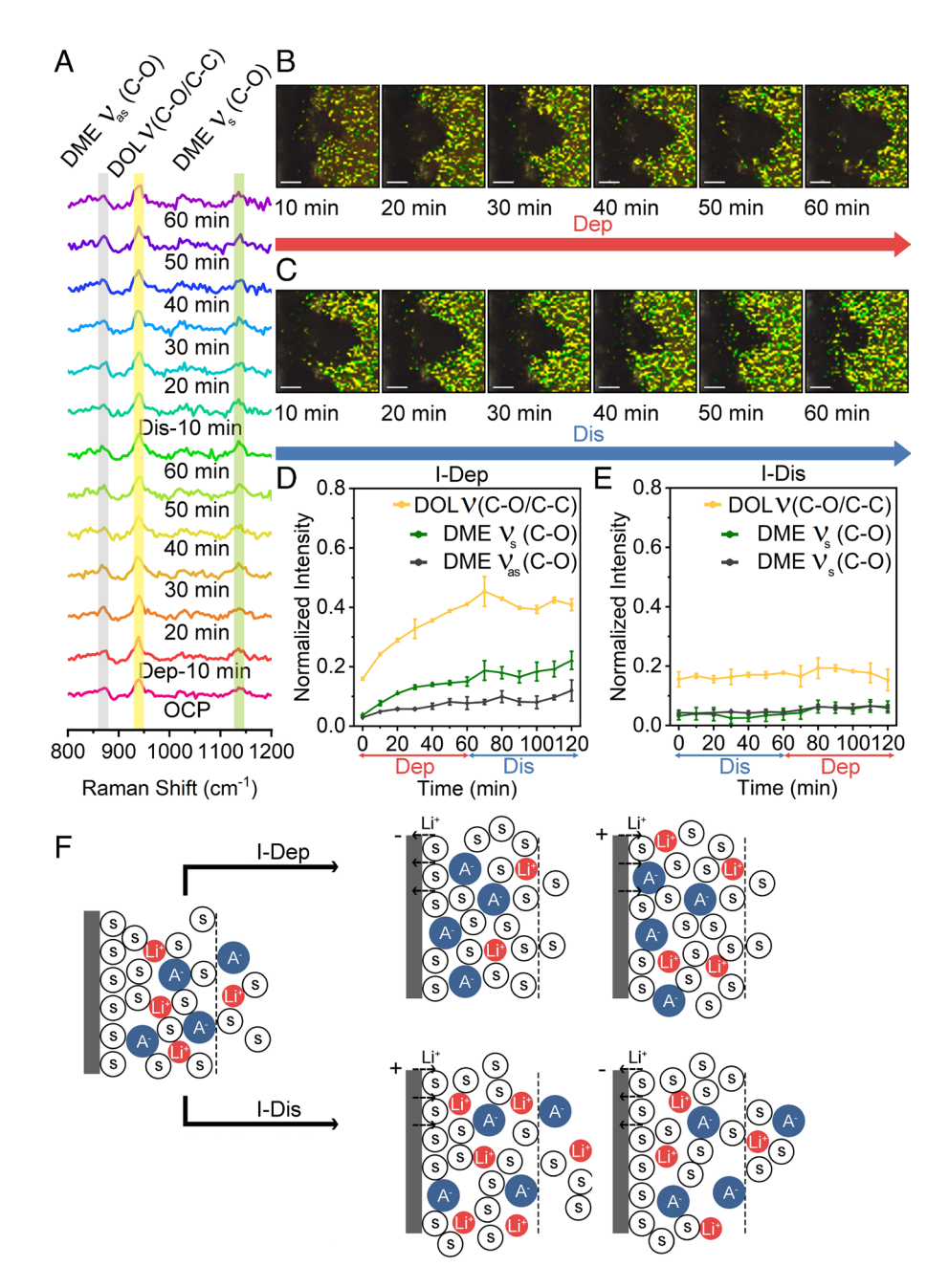


Fig. 6. Operando confocal Raman mapping of Li/electrolyte interfaces (evolution of the solvent) during Li deposition and dissolution. (A) Operando Raman spectra of the electrolyte near the Li metal (solvent regions). (B and C) Operando scans of the Li/electrolyte interfaces during deposition (B) and dissolution (C), respectively. In B and C, the yellow and green colors show the intensities of the peaks at 1,138 and 941 cm⁻¹, which represent DOL and DME, respectively. The scale bars are 30 µm. (D and E) Quantification of the average changes in normalized intensities vs. reaction time during the (D) I-Dep and (E) I-Dis processes. The SDs were drawn based on three sets of operando measurements. (F) Schematic explaining how the Li salt anions and solvent evolve during the different deposition and dissolution sequences.

species near the Li electrode, we found that the increase in anions and solvent fragments during the first deposition process plays a key role in interfacial stabilization. This points to the fact that more efforts should be devoted to interfacial protection during Li dissolution, especially for Li free cathode batteries, from the standpoints of regulation of ion transfer, electrolyte decomposition, and preprotection of the interfaces.

Conclusions

In this study, we provide compelling and direct evidence that shows the impact of the initial Li dissolution process on the distribution and evolution of the interfacial resistance, morphology,

conductivity, and electrolyte reactions at a Li metal anode. Using Li-S cells as a model system, we found that the overall cell resistance largely derives from the Li interfaces. The I-Dis of the Li metal leads to higher resistance and reduced uniformity. In situ AFM and SECM images clearly visualized the dramatically fast growth of the Li metal and evident break of the SEI in the I-Dis case compared with the I-Dep, which is likely the underlying cause of the significant increases in impedance. Cross-sections of the interfaces obtained using cryo-STEM show a more loose and diffuse SEI in the I-Dis case, while the I-Dep is more abrupt and compact. Furthermore, the dynamic responses of different electrolyte components near the Li electrode upon deposition/dissolution were visualized and analyzed using operando Raman imaging. The real-time decomposition of salt anions and release of free solvent near Li during the I-Dep are key to modifying the interface, enabling the species enrichment and structural compactness. These steps cannot be achieved during the I-Dis and even the following deposition processes, which can cause the deterioration of the interface in subsequent cycles. Our results have provided key insights into the Li dissolution mechanisms through multidimensional characterizations, enhancing our understanding of Li interfacial evolution and prompting a shift in our thinking to regulate the Li interface upon the I-Dis instead of the deposition process.

Materials and Methods

Battery Preparation. LiTFSI, DME, DOL, and sulfur were purchased from Sigma-Aldrich. Li₂S and Li foils were from Alfa-Aesar. For Li-S coin cells, sulfur electrodes were prepared by coating a slurry of sulfur: polyvinylidene fluoride: Super P (8:1:1) onto carbon paper (AvCarb EP40, Fuelcell Store). Li₂S₈ catholytes were used to assemble Li-polysulfide coin cells by mixing stoichiometric amounts of Li₂S and sulfur in 1.0 M LiTFSI in DOL/DME at 60 °C overnight. Li–Li symmetric coin cells were prepared using Li as the electrodes and 50 mM Li₂S₈, 1.0 M LiTFSI in DOL/DME as the electrolyte.

Three-Electrode Impedance Test. The three-electrode cell was purchased from MTI Corporation. By employing a separate RE, the contributions of the CE (Li in our case), to the potential response, can be identified and a more accurate and precise understanding of the electrochemistry occurring in the battery can be obtained. A four-electrode configuration was employed previously. The potential of the RE remained essentially constant throughout the discharge/charge processes, verifying the reliability of the RE used in our three-electrode cells (17). For the three-electrode Li-S cells, the WE, CE, and RE were S, Li, and Li, respectively. Three-electrode Li-Li-Li cells were employed for investigating the effects of Li deposition/dissolution processes. Potentiostatic EIS was performed on cells at different stages of the discharge/charge processes using a 10 mV amplitude and a frequency range from 10⁶ to 0.1 Hz, with a potentiostat (Biologic SP-200). DRT transformations were conducted by the MATLAB GUI tool box developed by Ciucci's research team (45). In addition, the values of the interfacial resistances were derived from the equivalent circuit (SI Appendix, Fig. S4) using the Zview software.

In Situ AFM. The cell for in situ AFM observation was assembled on a commercial AFM system (Bruker, Dimension Icon AFM with Nanoscope V controllers) coupled to an electrochemical workstation. All experiments were carried out in an argon-filled glovebox (MIKROUNA Glove box, Super 1220/750, H₂O < 0.1 ppm, $O_2 < 0.1$ ppm). The Li surface was scanned with a rectangular silicon AFM tip (force constant of 26 N m⁻¹) in PeakForce Quantitative Nanomechanics mode. The measurements of the roughness and volume were accomplished using Nanoscope Analysis.

SECM. For SECM measurements, 5 mM MV²⁺ was added to the electrolyte as the redox mediator. Molten Li was employed as the substrate, which was precleaned and flattened for scanning. A Pt microprobe with a diameter of circa (ca.) 10 µm was used as the tip electrode. Two Li strips were assembled into the cell as the CE and RE. The tip electrode was placed 200 μm above the substrate. A constant potential of 2.4 V vs. Li⁺/Li was applied when the tip approached the substrate. The tip approach will stop when the detected current is 70% lower or higher than the initial value, indicating negative or positive feedback, respectively. The SECM images were captured at this height over an area size of 200 \times 200 μm with the step size of 10 μm .The normalized tip current, I_T, and tip-to-substrate distance, L, were calculated from the tip current dividing the steady-state current and the travel distance divided by the tip radius, respectively.

- K. Xu, Electrolytes and interphases in Li-ion batteries and beyond. Chem. Rev. 114, 11503-11618
- J. B. Goodenough, K. S. Park, The Li-ion rechargeable battery: A perspective. J. Am. Chem. Soc. 135, 1167-1176 (2013).

Cryogenic STEM and EELS Characterization. Li-Li coin cells for both I-Dep and I-Dis cases were prepared for cryo-STEM characterization. In order to preserve the electrolyte and Li metal surface, the I-Dep and I-Dis Li-Li cells were opened and immediately plunge-frozen into slushed liquid nitrogen. Once the cells were vitrified, a cross-section of a dendritic site for each case was thinned to electron transparency using an Thermo Fisher (FEI) Strata 400s DualBeam, fitted with a Quorum PP3010T cryogenic scanning electron microscopy (cryo-SEM)/FIB system. The electron transparent samples were then transferred to an FEI Titan Themis STEM, operating at 300 kV, and cooled to -190 °C. During the entire sample preparation and transfer process, the lamella remained cooled to below -175 °C. All EELS measurements were collected using a Gatan imaging filter Tridiem energy filter and K2 Summit direct electron detector.

Operando Confocal Raman Microscopy Characterization. A 3-mm diameter hole was drilled in the middle of a 2032 coin cell casing for optical observation. A Raman transmissive film was then glued onto it to ensure a hermetic seal. Li-Li symmetric cells were used, where only one-half Li disk was employed on the observation side. The coin cells were assembled in an argon-filled glove box with oxygen and water levels below 0.1 ppm and 0.1 ppm, respectively. The Raman spectra and mapping images were obtained with a WITec Alpha300R confocal Raman microscope. The calibration of the spectra and color contrast of the images were set consistently for quantification and comparison; 20 cm⁻¹ regions centered around the peak positions on the spectra were selected for mapping. Areas in the Raman mapping were extracted and quantified by ImageJ. Upon electrochemical reactions, changes in the areas on the mappings were converted into corresponding normalized intensities to plot with time. Operando characterizations were achieved by controlling the reaction rate of the cells and monitoring the voltage-time responses with a potentiostat (Methrohm Autolab PGSTAT302N).

Ex Situ Characterization. During XPS, samples were analyzed using a Surface Science Instruments SSX-100 Electron Spectroscopy for Chemical Analysis spectrometer with operating pressure ca. 1×10^{-9} torr, with survey spectra collected at 150 eV pass energy and the high-resolution scans collected at 50 eV. A flood gun was used for charge neutralization. Data analysis was conducted by CasaXPS with Shirley as the background. All the samples were stored under Ar before XPS analysis. 7 Li and 17 O NMR spectra were acquired on a AV400 Bruker spectrometer at 50 °C.

Data, Materials, and Software Availability. All study data are included in the article and/or supporting information.

ACKNOWLEDGMENTS. We acknowledge support from the Cornell Energy System Institute, Daimler/Mercedes-Benz. The cryo-EM analysis was supported by the NSF (DMR-1654596) and the Packard Foundation. This work made use of the Raman, NMR, and electron microscopy facilities of the Cornell Center for Materials Research Shared Facilities which are supported through the NSF Materials Research Science and Engineering Centers (MRSEC) program (DMR-1719875). Additional support for the FIB/SEM cryo-stage and transfer system was provided by the Kavli Institute at Cornell and the Energy Materials Center at Cornell, Department of Energy Energy Frontier Research Center program in Basic Energy Sciences (DOE EFRC BES, DE-SC0001086). The Thermo Fisher Scientific (TFS)/FEI Titan Themis 300 was acquired through NSF MRI-1429155, with additional support from Cornell University, the Weill Institute, and the Kavli Institute at Cornell. R.W. acknowledges the support from the National Key R&D Program of China (Grant No. 2021YFB2500300) and CAS Project for Young Scientists in Basic Research (Grant No. YSBR-058). S.L. thanks Dr. Ivan Kereszetes and Tong-Tong Zuo for the helpful discussions.

Author affiliations: ^aDepartment of Chemistry and Chemical Biology, Cornell University, Ithaca, NY 14853; ^bSchool of Applied and Engineering Physics, Cornell University, Ithaca, NY 14853; ^cKavli Institute at Cornell, Cornell University, Ithaca, NY 14853; ^dKey Laboratory of Molecular Nanostructure and Nanotechnology, Beijing National Laboratory for Molecular Sciences, CAS Research/Education Center for Excellence in Molecular Sciences, Institute of Chemistry, Chinese Academy of Sciences, Beijing 100190, China; and eSchool of Chemical Sciences, University of Chinese Academy of Sciences, Beijing 100049, China

- 3. D. Lin, Y. Liu, Y. Cui, Reviving the lithium metal anode for high-energy batteries. Nat. Nanotechnol. 12, 194-206 (2017).
- X. B. Cheng, R. Zhang, C. Z. Zhao, Q. Zhang, Toward safe lithium metal anode in rechargeable batteries: A review. Chem. Rev. 117, 10403-10473 (2017).

- S. H. Yu, X. Feng, N. Zhang, J. Seok, H. D. Abruna, Understanding conversion-type electrodes for lithium rechargeable batteries. Acc. Chem. Res. 51, 273-281 (2018).
- F. N. Jiang et al., Mechanism understanding for stripping electrochemistry of Li metal anode SusMat 1, 506-536 (2021).
- X.-B. Cheng, J.-Q. Huang, Q. Zhang, Review-Li metal anode in working lithium-sulfur batteries. J. Electrochem. Soc. 165, A6058-A6072 (2017).
- X. B. Cheng et al., A review of solid electrolyte interphases on lithium metal anode. Adv. Sci. (Weinh) 3, 1500213 (2016).
- E. Peled, S. Menkin, Review-SEI: Past, present and future. J. Electrochem. Soc. 164, A1703-A1719 (2017)
- Y. Gu et al., Designable ultra-smooth ultra-thin solid-electrolyte interphases of three alkali metal anodes. Nat. Commun. 9, 1339 (2018).
- M. R. Busche et al., Dynamic formation of a solid-liquid electrolyte interphase and its consequences for hybrid-battery concepts. Nat. Chem. 8, 426-434 (2016).
- H. Cheng et al., Emerging era of electrolyte solvation structure and interfacial model in batteries. ACS Energy Lett. 7, 490-513 (2022).
- X. Chen, Q. Zhang, Atomic insights into the fundamental interactions in lithium battery electrolytes. Acc Chem. Res. 53, 1992-2002 (2020).
- J. Kasemchainan et al., Critical stripping current leads to dendrite formation on plating in lithium anode solid electrolyte cells. Nat. Mater. 18, 1105-1111 (2019).
- D. Koo, B. Kwon, J. Lee, K. T. Lee, Asymmetric behaviour of Li/Li symmetric cells for Li metal batteries. Chem. Commun. (Camb) 55, 9637-9640 (2019).
- H. Liu et al., Plating/stripping behavior of actual lithium metal anode. Adv. Energy Mater. 9, 1902254 (2019).
- 17. J. Seok, C. N. Gannett, S. H. Yu, H. D. Abruna, Understanding the impacts of Li stripping overpotentials at the counter electrode by three-electrode coin cell measurements. Anal. Chem. 93, 15459-15467 (2021).
- F. Shi et al., Lithium metal stripping beneath the solid electrolyte interphase. Proc. Natl. Acad. Sci. U.S.A. 115, 8529-8534 (2018).
- K. N. Wood et al., Dendrites and pits: Untangling the complex behavior of lithium metal anodes through operando video microscopy. ACS Cent Sci. 2, 790-801 (2016).
- Y. Zhang, F. M. Heim, N. Song, J. L. Bartlett, X. Li, New insights into mossy Li induced anode degradation and its formation mechanism in Li-S batteries. ACS Energy Lett. 2, 2696-2705 (2017).
- K. J. Harry, D. T. Hallinan, D. Y. Parkinson, A. A. MacDowell, N. P. Balsara, Detection of subsurface structures underneath dendrites formed on cycled lithium metal electrodes. Nat. Mater. 13, 69-73 (2014).
- F. Dion, A. Lasia, The use of regularization methods in the deconvolution of underlying distributions in electrochemical processes. J. Electroanal. Chem. 475, 28-37 (1999).
- Y. Lu et al., The carrier transition from Li atoms to Li vacancies in solid-state lithium alloy anodes. Sci. Adv. 7, eabi5520 (2021).
- 24. A. Kushima et al., Liquid cell transmission electron microscopy observation of lithium metal growth and dissolution: Root growth, dead lithium and lithium flotsams. Nano Energy 32, 271–279 (2017).
- 25. P. Bai, J. Li, F. R. Brushett, M. Z. Bazant, Transition of lithium growth mechanisms in liquid
- electrolytes. *Energy Environ. Sci.* **9**, 3221–3229 (2016).
 26. A. J. Bard, F. R. F. Fan, J. Kwak, O. Lev, Scanning electrochemical microscopy. Introduction and principles. Anal. Chem. 61, 132-138 (1989).

- 27. D. Polcari, P. Dauphin-Ducharme, J. Mauzeroll, Scanning electrochemical microscopy A comprehensive review of experimental parameters from 1989 to 2015. Chem. Rev. 116, 13234-13278 (2016).
- Z. J. Barton, J. Rodriguez-Lopez, Emerging scanning probe approaches to the measurement of ionic reactivity at energy storage materials. *Anal. Bioanal. Chem.* **408**, 2707–2715 (2016).
- X. Zeng et al., In situ observation of interface evolution on a graphite anode by scanning electrochemical microscopy. ACS Appl. Mater. Interfaces 12, 37047–37053 (2020).
 S. Liu et al., Understanding the cathode electrolyte interface formation in aqueous electrolyte by
- scanning electrochemical microscopy. *J. Mater. Chem. A* **7**, 12993–12996 (2019).

 31. H. Bulter, F. Peters, J. Schwenzel, G. Wittstock, Spatiotemporal changes of the solid electrolyte
- interphase in lithium-ion batteries detected by scanning electrochemical microscopy. Angew. Chem. Int. Ed. Engl. 53, 10531-10535 (2014).
- M. J. Zachman, E. Asenath-Smith, L. A. Estroff, L. F. Kourkoutis, Site-specific preparation of intact solid-liquid interfaces by label-free in situ localization and cryo-focused ion beam lift-out. Microsc. Microanal. 22, 1338-1349 (2016).
- S. Rubino et al., A site-specific focused-ion-beam lift-out method for cryo transmission electron microscopy. J. Struct. Biol. 180, 572-576 (2012).
- M. J. Zachman, Z. Tu, S. Choudhury, L. A. Archer, L. F. Kourkoutis, Cryo-STEM mapping of solid-liquid interfaces and dendrites in lithium-metal batteries. Nature 560, 345-349 (2018).
- Q. Cheng et al., Operando and three-dimensional visualization of anion depletion and lithium growth by stimulated Raman scattering microscopy. Nat. Commun. 9, 2942 (2018).
- E. Miele et al., Hollow-core optical fibre sensors for operando Raman spectroscopy investigation of Li-ion battery liquid electrolytes. Nat. Commun. 13, 1651 (2022).
- M. Hagen et al., In-situ Raman investigation of polysulfide formation in Li-S cells. J. Electrochem. Soc. 160, A1205-A1214 (2013).
- P. Dubois, J. P. Lelieur, G. Lepoutre, Identification and characterization of lithium polysulfides in solution in liquid ammonia. Inorg. Chem. 27, 73-80 (1988).
- R. Bouchal, A. Boulaoued, P. Johansson, Monitoring polysulfide solubility and diffusion in fluorinated ether-based electrolytes by operando raman spectroscopy. Batter. Supercaps 3, 397-401 (2020).
- L. Suo, F. Zheng, Y.-S. Hu, L. Chen, FT-Raman spectroscopy study of solvent-in-salt electrolytes. Chin. Phys. B 25, 016101 (2016).
- W. Zhu et al., Investigation of the reaction mechanism of lithium sulfur batteries in different electrolyte systems by in situ Raman spectroscopy and in situ X-ray diffraction. Sustain. Energy Fuels **1**, 737-747 (2017).
- 42. X. Chen, H. R. Li, X. Shen, Q. Zhang, The origin of the reduced reductive stability of ion-solvent complexes on alkali and alkaline earth metal anodes. Angew. Chem. Int. Ed. Engl. 57, 16643-16647
- X. O. Zhang et al., Electrolyte structure of lithium polysulfides with anti-reductive solvent shells for practical lithium-sulfur batteries. Angew. Chem. Int. Ed. Engl. 60, 15503–15509 (2021).
- Q. Liu, F. Wu, D. Mu, B. Wu, Comparative calculation on Li+ solvation in common organic electrolyte Solvents for lithium ion batteries*. Chin. Phys. B 29, 048202 (2020).

 T. H. Wan, M. Saccoccio, C. Chen, F. Ciucci, Influence of the Discretization Methods on the
- Distribution of Relaxation TimesDeconvolution: Implementing Radial Basis Functions with DRTtools. Electrochimica Acta 184, 483-499 (2015).